

## Stopping Powers and Ranges of 5–90-MeV S<sup>32</sup>, Cl<sup>35</sup>, Br<sup>79</sup>, and I<sup>127</sup> Ions in H<sub>2</sub>, He, N<sub>2</sub>, Ar, and Kr: A Semiempirical Stopping Power Theory for Heavy Ions in Gases and Solids\*

T. E. PIERCE AND MARSHALL BLANN

*Department of Chemistry and Nuclear Structure Laboratory, University of Rochester, Rochester, New York*

(Received 6 May 1968)

Stopping powers and range curves for approximately 5–90-MeV beams of S<sup>32</sup>, Cl<sup>35</sup>, Br<sup>79</sup>, and I<sup>127</sup> in H<sub>2</sub>, He, N<sub>2</sub>, Ar, and Kr are presented. Polynomial fits to the range curves followed by differentiation showed the  $\Delta E/\Delta X$  measurements to be equivalent to  $dE/dX$  to within experimental uncertainties. The experimental stopping powers are estimated to have errors no greater than  $\pm 3\%$  for S<sup>32</sup> and Cl<sup>35</sup>,  $\pm 4\%$  for Br<sup>79</sup>, and  $\pm 5\%$  for I<sup>127</sup>. Integral ranges should be accurate to  $\pm 1\%$  or better. Small corrections for nuclear stopping were applied to the stopping powers, and the resulting stopping powers were analyzed in terms of fractional effective charge, defined as the quotient of the charge giving the correct stopping power in the Bethe equation to the nuclear charge, using experimental proton stopping powers. The same was done for published heavy-ion stopping powers in solids (Be, C, Al, Ni, Ag, and Au); and the fractional effective charges  $\gamma$  were compared against a reduced velocity parameter  $v_r = v/(v_0 Z^{2/3})$ , where  $v$  is the ion laboratory velocity and  $v_0 Z^{2/3}$  is the Thomas-Fermi electron velocity. All data so analyzed fell on a single smooth curve of  $\gamma$  versus  $v_r$  to  $\pm 3\%$ , with the exception of some of the data taken in H<sub>2</sub>. The curve may be parametrized as  $\gamma = [1 - \exp(-0.95 v_r)]$ . For the reduced velocity region  $v_r \geq 0.1$ , electronic stopping powers may be computed from the semiempirical relationship

$$(dE/dX)_{Z,A,E} = (dE/dX)_{p,E/A} Z^2 [1 - \exp(-0.95 v_r)]^2 [1 - \exp(-2.5 v_p)]^{-2},$$

where  $Z$ ,  $A$ , and  $E$  represent the atomic number, mass number, and kinetic energy of the heavy ion; the  $dE/dX$  factor subscripted  $p$ ,  $E/A$  denotes the experimental proton stopping power for protons of energy  $E/A$ ;  $v_r$  is the reduced velocity of the heavy ion; and  $v_p$  is the proton velocity in units of MeV<sup>1/2</sup>. To the extent that the extrapolations of the correlations found in this work are valid, stopping powers so calculated should be accurate to  $\pm 8\%$ . The effective charge parameter for gases and solids is approximately equivalent to the root-mean-square (rms) charge for the same ions in gas. The effective charges for heavy ions in solids are thus shown to differ markedly from the rms charges measured for solid stripping foils. These data suggest that the extra electrons are bound while the ion is in the solid and are lost when the ion leaves the stripping foil.

### I. INTRODUCTION

WE present results of measurements of energy loss per unit path length,  $\Delta E/\Delta X$ , for beams of S<sup>32</sup>, Cl<sup>35</sup>, Br<sup>79</sup>, and I<sup>127</sup> in H<sub>2</sub>, He, N<sub>2</sub>, Ar, and Kr. The energy range investigated was approximately 5–90 MeV. The investigation was undertaken for several reasons; one of these was the lack of published gas stopping powers of comparable accuracy for these ions over the energy span of this work, a region for which no suitable stopping-power theory is available. The second was to provide accurate gas stopping data to compare with available data in solids to determine whether or not the physical state of the stopping medium influences its stopping power. While it has long been known that equilibrium charge states of heavy ions of a given velocity may vary greatly between stopping in gases and solids,<sup>1–4</sup> it has not been demonstrated experimentally that this affects the stopping powers as the functional dependence on charge of the Bethe-Block stopping theory would predict. We also wished to look for semiempirical

correlations in a large body of accurate stopping-power data, in the hope that such correlations would permit reliable interpolation and extrapolation of as yet unmeasured combinations of heavy-ion beams and stopping media. Finally, it is hoped that these and related data will eventually lead to improved theories of heavy-ion ranges and stopping powers.

We will first describe the experimental details and provide the  $\Delta E/\Delta X$  and energy-versus-thickness data, since these will be of prime interest to many. We next will explore the relationship between an effective charge to be defined with respect to the Bethe-Block stopping equation and the velocity of the heavy ions in various stopping media, including solids. In the latter section, any differences between stopping in solids and gases will be explored; and a correlation of stopping-power data will be discussed for both solid and gaseous stopping media. An analytic expression will be presented which will allow calculation of heavy-ion stopping powers using proton stopping powers as input, and the relationship between rms and effective charges of heavy ions in gases and solids will be discussed.

### II. EXPERIMENTAL PROCEDURES

#### A. Ion Acceleration and Transport

The ion beams were produced on the University of Rochester MP tandem Van de Graaff accelerator. The

\* Work supported by the U.S. Atomic Energy Commission.

<sup>1</sup> E. Almquist, C. Broude, M. A. Clark, J. A. Kuehner, and A. E. Litherland, *Can. J. Phys.* **40**, 954 (1962).

<sup>2</sup> L. Grodzins, R. Kalish, D. Murnick, R. J. Van de Graaff, F. Chmara, and P. H. Rose, *Phys. Letters* **24B**, 282 (1967).

<sup>3</sup> C. D. Moak, H. O. Lutz, L. B. Bridwell, L. C. Northcliffe, and S. Datz, *Phys. Rev. Letters* **18**, 41 (1967).

<sup>4</sup> H. D. Betz, G. Hortig, E. Leischner, Ch. Schmelzer, B. Stadler, and J. Wehrauch, *Phys. Letters* **22**, 643 (1966).

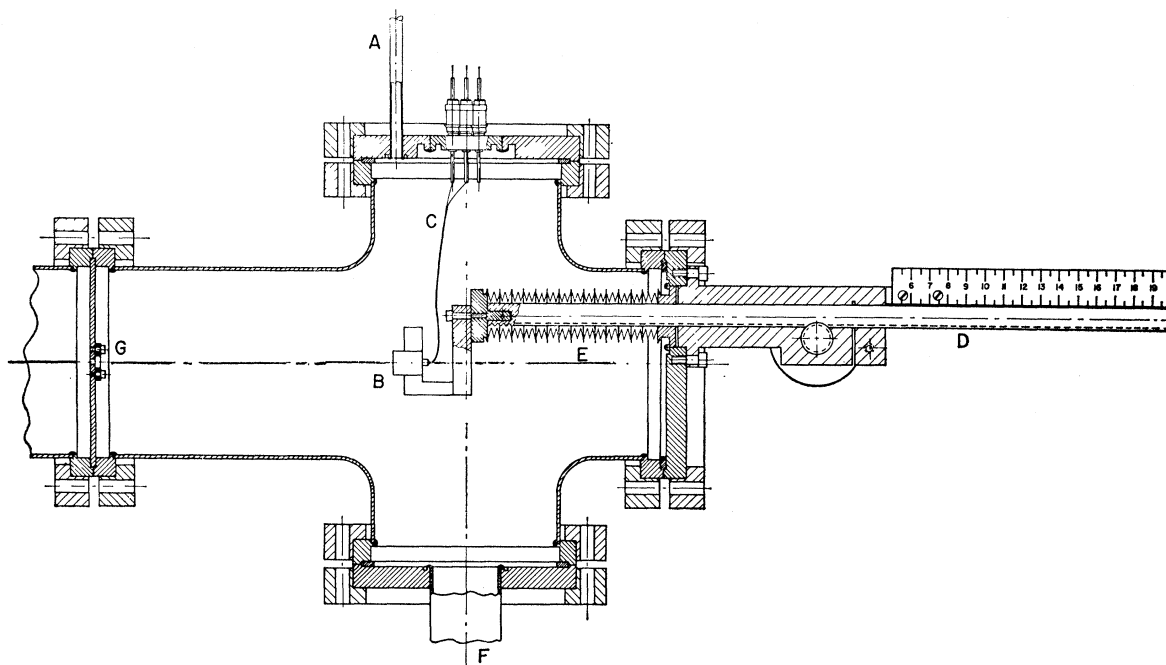


FIG. 1. Experimental apparatus for  $\Delta E/\Delta X$  measurement. The diagram is a cross-sectional area of a plane through the beam axis. The beam enters the chamber through a 3-mm aperture at G, where a retaining ring for a thin window is screwed down. The radiation detector is at B on a lucite mount connected to a movable arm D (rack and pinion controlled) with vacuum seal through the bellows E. A millimeter scale is affixed above D, with a vernier scale on the end of the movable arm D (not shown). The manometer and filling connection are at A; electrical feedthroughs are at C; and the manifold for pumping the chamber is at F. The beam line diameter, which is the gas-cell diameter, is 10 cm; the length of the gas cell is  $\sim 30$  cm; the detector could be positioned anywhere between 1.9 and 17 cm from the window at G.

beams were extracted from the standard hydrogen duoplasmatron source, with either solids (several mg) such as S,  $\text{NH}_4\text{Cl}$ ,  $\text{NH}_4\text{Br}$ , or  $\text{NH}_4\text{I}$ , or gaseous impurities such as  $\text{H}_2\text{S}$ ,  $\text{HCl}$ ,  $\text{HBr}$ , or  $\text{HI}$  being added to the source cavity. The machine was run in a stabilized mode for all experiments, with terminal potentials between 2 and 10 MV. Single energy components of the beam were transported through a  $90^\circ$  analyzing magnet. A switching magnet following the analyzer was used to bend the beams an additional  $45^\circ$  into the beam line on which the measurements were performed. Careful control of the current in the switching magnet, plus defocusing in the magnetic quadrupole lens preceding the analyzing magnet, permitted acceptably low beam currents to be directed into the experimental apparatus.

### B. Experimental Apparatus

The chamber used for these measurements is diagrammed in Fig. 1. The unit was at the end of the  $45^\circ$  beam line, approximately 7 m from the switching magnet. The radiation detectors (Ortec fission-fragment detectors) could be set for distances between  $\sim 1.9$  and 17 cm from the Mylar window. The window diameter was 3 mm; detectors were 1 cm diam. Distances were read with a millimeter scale using the end of the detector arm as a reference point during the early experiments

( $\pm 0.2$ -mm precision); a vernier was used on the end of the detector arm for the majority of the measurements ( $\pm 0.1$ -mm precision). The detector was ordinarily moved 2-3 cm at a time during data acquisition. Gas pressures were read with a mercury manometer, with estimated accuracy of  $\pm 0.25$  mm. Pressures used varied between 23 and 255 mm of mercury. Changes in volume due to the position of the bellows on which the detector arm was mounted caused a change in pressure of up to 1.5% between the minimum and maximum detector to window distances. Appropriate corrections were applied.

### C. Data Acquisition and Reduction

Pulses due to the heavy-ion beams were recorded as 2048-channel pulse-height spectra, using the on-line PDP-8/6 computer system. For each of the four beam-particle types investigated, a detector calibration was run without Mylar windows (see Fig. 1) with incident ion energies in the general range 5 to 100 MeV. Six to 10 energies were run for each beam to allow an adequate determination of slope and linearity. Aluminized or gold-coated Mylar windows were then placed over the aperture (see Fig. 1) with an indium seal, and beams of the incident energies to be used for gas  $\Delta E/\Delta X$  measurements were put through the Mylar

TABLE I. Purities of gases used in stopping-power measurements.

Gas	Purity (%)
Hydrogen	99.9
Helium	99.99
Nitrogen	99.9
Argon	99.5
Krypton	99.5

windows. This gave the energy loss through the windows and the incident energies of the ions on the gases when the chamber had been filled. The windows used in the first few measurements were  $529 \mu\text{g}/\text{cm}^2$ , including  $\sim 20 \mu\text{g}/\text{cm}^2$  of aluminum coating; the majority of measurements were made through  $335\text{-}\mu\text{g}/\text{cm}^2$  Mylar windows having a  $7\text{-}\mu\text{g}/\text{cm}^2$  gold coating. The energy losses in these windows have been discussed elsewhere.<sup>5</sup>

Following the detector calibration and determination of beam energies through the Mylar window, the chamber was filled to the desired pressure with the gas being studied. Gas purities are listed in Table I. A minimum of 20 min was allowed to pass for temperature equilibration before proceeding; room temperatures were noted to  $\pm 0.2^\circ\text{C}$ . Beam-energy measurements were then made at successively greater detector to window distances, each distance requiring 2 to 5 min for data collection, with count rates kept under 100 per sec. At these counting rates, there were no measurable heating effects in the gas. Several runs were made at unusually low or unusually high gas pressures to check for pressure dependence and charge-state effects on  $\Delta E/\Delta X$ ; these data are discussed in greater detail further on in this report. At the gas pressures used, there was no deviation greater than 0.5% from ideality, as calculated using the Van der Waal's gas law; we, therefore, assumed perfect gases in converting pressure and path length to thickness in  $\mu\text{g}/\text{cm}^2$ . Typical pulse-height spectra for detector calibration and for measuring  $\Delta E/\Delta X$  are illustrated in Fig. 2.

Pulse-height-versus-energy responses for calibration were computed by least-square analyses, with all experimental points lying within  $\pm 100$  keV of the least-square line. In the case of  $\text{Br}^{79}$  and  $\text{I}^{127}$  ions, the energy loss in the  $40\text{-}\mu\text{g}/\text{cm}^2$  detector window made it necessary to use two line segments to fit the calibration points to within  $\pm 100$  keV; one segment for  $E \leq 40$  MeV, the other for  $E \geq 40$  MeV. A Gaussian least-squares program was used to find the channel number of the peak centers and, therefore, the mean energy. These values were always within one-half channel of the value found from the center of the peak at half-maximum, i.e., within  $\pm 25$  keV. Full widths at half-maximum of the pulse-height responses for ions in gas varied between 600 keV for  $\text{S}^{32}$  ions and 3 MeV for  $\text{I}^{127}$ . The

<sup>5</sup> T. E. Pierce, W. W. Bowman, and M. Blann, Phys. Rev. 172, 287 (1968).

standard deviations of the peak widths and numbers of events in the peaks were used to compute the uncertainties in peak positions to 90% confidence limits; all peak centers were known to  $\pm 25$  keV when these confidence limits were applied. Pulsers were run with each spectrum to indicate any gain change; this generally was less than the pulse generator fluctuation,  $\pm 50$  keV. On a few occasions, drifts of up to 2% in gain were detected and corrected for.

The  $\Delta E/\Delta X$  values measured are presented in Tables II-V and in Figs. 3-6. The  $\Delta E$  values for each point are also presented in the tables; energies in Tables II-V and Figs. 3-6 are mean energies. The curves of energy versus thickness traversed (the mirror image of the range-energy curves) are shown in Figs. 7-13. In Figs. 3-6, the first point of each set of measurements is not presented, i.e., the point for which the ion passes through the window and first segment of gas. There are several reasons for this point being considered less reliable than the others. First, it is possible that the Mylar window bends slightly because of the addition of gas to the cell; since energy losses of 6-30 MeV occurred in the window and since  $\Delta E$  values as low as 1-2 MeV are measured in the gas cell, a very small bowing of the window could produce a change in energy of several hundred keV over that through the window when both sides were under vacuum. Second, equilibrium charge states in solids are known to be greater than those in gases so that the ions leaving the window and entering the gas will have higher than their equilibrium charge in

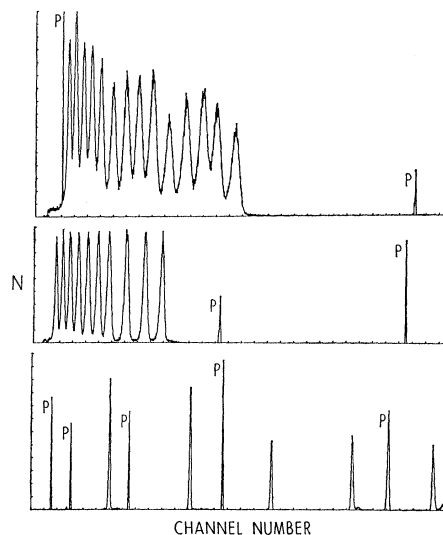


FIG. 2. Typical pulse-height response curves for detector calibration and  $\Delta E/\Delta X$  measurement. The ordinate "N" is a relative intensity scale; the abscissa (channel number) is proportional to energy, where all three spectra correspond approximately to the range 0-100 MeV. All peaks marked "P" are due to a pulse generator. The bottom curve is a detector calibration spectrum for  $\text{S}^{32}$  ions; the middle spectrum is for  $\text{Cl}^{35}$  ions in Ar, where the incident  $\text{Cl}^{35}$  energy was 29.37 MeV; the top spectrum is for  $\text{I}^{127}$  ions in  $\text{H}_2$ , where the incident  $\text{I}^{127}$  ions were 120 MeV.

TABLE II. Stopping powers of sulfur ions in gases.

$\bar{E}$ (MeV)	$\Delta E/\Delta X$ (keV cm <sup>2</sup> /μg)	$\Delta E$ (MeV)	$\bar{E}$ (MeV)	$\Delta E/\Delta X$ (keV cm <sup>2</sup> /μg)	$\Delta E$ (MeV)	$\bar{E}$ (MeV)	$\Delta E/\Delta X$ (keV cm <sup>2</sup> /μg)	$\Delta E$ (MeV)	$\bar{E}$ (MeV)	$\Delta E/\Delta X$ (keV cm <sup>2</sup> /μg)	$\Delta E$ (MeV)
Hydrogen (238 mm)			45.35	29.5	1.96	Nitrogen (43 mm)			Argon (23 mm)		
91.83	51	2.21 <sup>a</sup>	42.08	29.9	4.57	92.51	16.1	2.66 <sup>a</sup>	69.31	12.3	1.15 <sup>a</sup>
87.90	54	5.65	37.47	30.7	4.67	88.73	16.8	4.90	68.30	11.5	0.88
83.23	47	3.71	32.77	31.2	4.72	84.86	16.2	2.85	65.72	12.5	4.40
78.58	53	5.56	28.01	31.8	4.79	81.95	17.0	6.07	61.24	13.0	4.56
73.29	55	5.02	23.94	31.7	3.16	78.92	17.8	3.11	58.90	12.9	1.21 <sup>a</sup>
71.15	81	3.23 <sup>a</sup>	26.53	32.2	3.07 <sup>a</sup>	75.90	16.9	2.93	57.12	12.7	0.83
67.96	60	3.15	23.95	31.8	2.11	71.39	17.6	6.08	55.20	12.8	4.52
64.70	64	3.36	20.48	31.6	4.83	71.98	18.3	3.02 <sup>a</sup>	50.65	13.0	4.57
61.45	60	3.15	15.79	29.8	4.54	69.43	18.1	2.09	48.44	15.7	1.47 <sup>a</sup>
58.18	65	3.38	11.51	26.5	4.02	66.77	18.3	3.22	47.38	10.2	0.67 <sup>b</sup>
54.75	67	3.47	7.87	21.7	3.27	63.52	18.6	3.28	44.71	13.3	4.67
51.25	68	3.54	Krypton (120 mm)			58.52	19.3	6.73	40.04	13.3	4.67
47.62	72	3.72	88.19	10.6	9.57 <sup>a</sup>	51.71	19.8	6.88	37.98	13.3	1.24 <sup>a</sup>
50.00	88	3.83 <sup>a</sup>	80.84	9.1	5.03	51.30	20.7	3.42 <sup>a</sup>	36.91	13.9	0.91
46.10	75	3.95	75.92	8.8	4.82	48.43	20.1	2.32	35.41	13.9	2.09
42.14	76	3.98	71.05	9.0	4.92	45.43	21.0	3.69	33.00	13.6	2.73
38.06	80	4.18	66.10	9.1	4.99	41.74	20.9	3.67	30.25	13.8	2.77
33.81	83	4.33	61.10	9.1	4.99	36.11	21.8	7.61	27.84	13.5	2.04
29.38	87	4.52	56.07	9.3	5.08	29.37	22.5	5.87	27.43	13.6	1.27 <sup>a</sup>
24.86	87	4.52	51.00	9.3	5.06	23.43	23.3	6.01	26.35	13.9	0.91
20.28	90	4.63	45.92	9.4	5.10	30.28	22.5	3.73 <sup>a</sup>	24.82	14.2	2.14
28.63	115	4.55 <sup>a</sup>	40.81	9.4	5.12	27.10	23.0	2.65	22.33	14.1	2.84
24.01	89	4.71	35.72	9.3	5.06	23.71	23.5	4.13	19.49	14.1	2.84
19.35	89	4.69	30.67	9.3	5.03	19.62	23.0	4.04	17.03	13.8	2.08
15.28	86	3.37	25.67	9.2	4.99	13.78	21.9	7.64	16.95	14.8	1.38 <sup>a</sup>
12.06	78	3.07	20.72	9.1	4.90	8.37	18.3	2.18	15.83	13.3	0.87
9.20	67	2.64	15.89	8.8	4.76	5.69	12.6	2.18	14.31	14.3	2.16 <sup>b</sup>
7.16	55	1.44	Krypton (24 mm)			Nitrogen (57 mm)			11.88	13.4	2.70
5.47	51	1.97	91.56	16.5	2.73 <sup>a</sup>	68.70	20.0	2.50 <sup>a</sup>	8.47	11.7	4.12
3.89	29.9	1.16	88.45	8.0	3.51 <sup>b</sup>	66.66	18.3	1.59	7.46	11.7	1.00 <sup>a</sup>
Helium (233 mm)			84.87	8.2	3.63 <sup>b</sup>	63.42	18.3	4.89	6.65	10.1	1.02
68.72	25.9	2.47 <sup>a</sup>	81.09	9.0	3.95	57.87	18.7	6.20	5.55	9.9	1.15
66.63	25.8	1.71	77.96	5.9	2.29 <sup>b</sup>	51.42	20.4	6.71	4.41	7.4	1.12
63.75	25.9	3.96	26.04	11.8	9.74 <sup>a</sup>	47.41	20.3	2.54 <sup>a</sup>	3.53	6.4	6.64
59.78	26.7	4.06	19.76	10.2	2.81 <sup>b</sup>	45.72	21.0	1.83	2.90	6.1	0.61
55.71	27.0	4.09	17.14	8.9	2.44	42.73	20.7	4.16			
51.55	28.0	4.22	13.97	8.9	3.90	38.52	21.4	4.27			
48.02	28.5	2.84	10.00	9.2	4.05	32.61	28.4	7.53 <sup>a</sup>			
47.75	29.9	2.85 <sup>a</sup>	6.73	5.7	2.49	25.44	26.0	6.81 <sup>b</sup>			

<sup>a</sup> First segment of gas following the window.<sup>b</sup> Outside experimental error for unknown causes.

the gas. This could affect the measured energy loss if  $dE/dX \propto Z^2$ , as predicted by the Bethe stopping-power equation.<sup>6</sup> Finally, the distance between the window and detector needed to calculate  $\Delta X$  for the first point in each series had to be estimated by measuring several distances with a ruler, whereas distances between successive points were obtained by difference between positions of the millimeter scale shown in Fig. 1. Additionally, a few other  $\Delta E/\Delta X$  values of Tables II-V are well outside experimental uncertainties and were not reproduced in Figs. 3-6. These values are indicated in Tables II-V.

Energies incident on the gas cell were usually selected so as to give some overlap between the highest value of one set of measurements and the lowest few values of the preceding set. The lower limit on energies for which measurements were made in the gas cell was not

allowed to get too low since this increased chances of accidental radiation damage to the detector. The upper energy limits were, of course, set by the 10-MV limit on terminal voltage, ion-source intensities, and charge-state distributions at the terminal stripping canal for the ions of interest.

The energy-versus-thickness curves of Figs. 7-13 were constructed from the data of Tables II-V by joining smoothly the overlapping regions of successive sets of  $\Delta E$ -versus-thickness measurements; all data used are presented in Tables II-V. The points of Figs. 7-13 were obtained from summing of the differential energy-loss data and were checked against the integral measurements, i.e., the maximum  $\Delta E$  and path length for any set of measurements was checked against the sums of smaller increments to be certain that there was no accumulation of errors. The range curves of Figs. 7-13 should have errors of  $\leq 1\%$ .

Polynomial least-square fits were made to segments of the energy-versus-thickness curves of Figs. 7-13. First

<sup>6</sup> H. A. Bethe and J. Ashkin, in *Experimental Nuclear Physics*, edited by E. Segré (John Wiley & Sons, Inc., New York, 1953), Vol. I.

TABLE III. Stopping power of chlorine ions in gases.

$\bar{E}$ (MeV)	$\Delta E/\Delta X$ (keV cm <sup>2</sup> /μg)	$\Delta E$ (MeV)	$\bar{E}$ (MeV)	$\Delta E/\Delta X$ (keV cm <sup>2</sup> /μg)	$\Delta E$ (MeV)
Hydrogen (230 mm)					
91.48	63	2.87 <sup>a</sup>	91.59	18.5	2.66 <sup>a</sup>
88.32	57	3.46	88.58	19.0	3.37
84.18	63	4.83	84.81	18.1	4.17
79.28	65	4.95	80.51	19.3	4.43
73.33	69	6.96	75.36	19.3	5.87
67.09	75	5.52	70.09	20.5	4.66
71.01	77	3.21 <sup>a</sup>	71.18	19.9	2.86 <sup>a</sup>
67.23	72	4.35	67.92	20.7	3.66
18.44	108	4.59 <sup>a</sup>	63.70	20.8	4.78
14.66	91	2.96	58.93	20.8	4.76
12.19	80	1.98	53.30	21.4	6.51
10.27	75	1.87	47.54	22.1	5.01
8.47	69	1.72	50.45	22.6	3.24 <sup>a</sup>
7.06	64	1.10	46.88	22.1	3.90
6.00	59	1.03	42.26	22.9	5.25
5.02	53	0.92	36.98	23.6	5.41
4.18	42.1	0.77	30.65	23.8	7.25
3.44	40.9	0.70	24.27	24.3	5.51
Helium (230 mm)					
91.83	23.1	2.18 <sup>a</sup>	29.60	24.4	3.50 <sup>a</sup>
89.24	25.8	3.00	25.65	24.8	4.39
85.76	26.2	3.95	20.66	24.3	5.59
81.87	25.7	3.85	15.23	23.0	5.28
77.24	27.1	5.39	11.81	20.5	1.57
72.47	28.0	4.15	10.27	19.7	1.51
71.34	26.9	2.53 <sup>a</sup>	8.85	17.8	1.33
68.44	28.2	3.28	7.56	16.1	1.23
64.52	29.7	4.48	6.35	15.8	1.21
60.11	29.5	4.42	5.33	11.1	0.82
56.85	31.7	6.11	Nitrogen (54 mm)		
49.49	31.1	4.60	18.71	28.4	4.03 <sup>a</sup>
50.61	30.9	2.91 <sup>a</sup>	15.42	23.7	2.56
47.33	31.5	3.66	12.77	22.0	2.74
43.06	32.3	4.87	10.18	19.6	2.45
38.20	32.4	4.86	8.20	18.1	1.49
32.44	33.5	6.66	6.80	15.9	1.32
26.69	32.7	4.84	5.55	14.4	1.18
29.80	32.9	3.10 <sup>a</sup>	4.45	12.3	1.02
26.33	33.1	3.84	3.53	10.2	0.83
22.00	32.0	4.83	Argon (50 mm)		
17.32	30.1	4.52	91.67	12.2	2.49 <sup>a</sup>
13.67	27.9	2.78	88.83	12.8	3.20
11.63	26.2	1.30	85.17	12.7	4.13
10.36	25.2	1.25	80.98	13.0	4.24
8.65	21.9	2.17	76.09	12.8	5.55
7.08	19.5	0.96	71.15	13.4	4.32
19.15	33.6	3.15 <sup>a</sup>	71.31	12.7	2.59 <sup>a</sup>
16.59	30.3	1.98	68.32	13.6	3.40
14.53	28.5	2.14	64.41	13.6	4.42
12.47	26.5	1.98	59.98	13.7	4.44
10.55	24.9	1.86	54.78	13.8	5.96
8.78	22.6	1.68	49.54	14.0	4.52
7.41	21.5	1.06	50.65	14.0	2.85 <sup>a</sup>
6.41	19.2	0.95	47.47	13.9	3.49
5.51	17.1	0.84	43.42	14.2	4.63
4.69	16.0	0.79	38.79	14.2	4.62
3.98	13.2	0.65	33.34	14.5	6.28
Argon (51 mm)					
19.02	16.4	3.43 <sup>a</sup>	27.90	14.3	4.60
16.18	15.3	2.24	29.87	14.5	2.96 <sup>a</sup>
13.83	14.7	2.46	26.57	14.5	3.63
11.46	13.6	2.28	22.30	15.1	4.92
9.60	12.8	1.44	18.64	14.8	2.40
8.22	12.0	1.32	16.26	14.5	2.36
6.95	10.9	1.22	13.57	14.1	3.03
5.89	10.1	1.11	10.98	13.1	2.13
4.76	8.4	0.94	8.94	12.3	1.96
3.86	7.9	0.86	7.37	10.8	1.18
			6.86	9.6	1.04

<sup>a</sup> First segment of gas following the window.

TABLE IV. Stopping power of bromine ions in gases.

$\bar{E}$ (MeV)	$\Delta E/\Delta X$ (keV cm <sup>2</sup> /μg)	$\Delta E$ (MeV)	$\bar{E}$ (MeV)	$\Delta E/\Delta X$ (keV cm <sup>2</sup> /μg)	$\Delta E$ (MeV)
Hydrogen (255 mm)					
44.31	259	10.40 <sup>a</sup>	75.48	61	7.39 <sup>a</sup>
34.07	168	10.07	69.96	54	3.65
24.30	129	9.47	65.14	53	5.99
16.02	83	7.11	59.22	52	5.85
20.18	128	5.14 <sup>a</sup>	53.43	51	5.74
16.03	90	3.16	47.78	49.2	5.56
13.18	69	2.54	42.30	47.9	5.39
10.55	55	2.71	37.06	45.2	5.10
8.21	40.3	1.98	32.12	42.4	4.78
Helium (205 mm)					
76.23	81	5.90 <sup>a</sup>	27.55	38.6	4.38
71.13	68	4.30	23.48	33.5	3.78
66.60	71	4.76	46.08	58	6.98 <sup>a</sup>
61.94	68	4.55	40.12	46.8	4.93
57.44	67	4.46	36.11	41.1	3.09
53.06	65	4.30	31.95	46.4	5.23 <sup>b</sup>
48.82	63	4.18	27.08	39.4	4.45
44.69	62	4.08	22.41	32.9	4.95
40.82	55	3.65	17.83	27.9	4.20
37.14	57	3.73	14.09	21.8	3.28
47.00	71	5.12 <sup>a</sup>	11.46	17.5	1.98
42.58	59	3.72	9.63	15.0	1.69
39.46	56	2.53	20.56	36.6	4.41 <sup>a</sup>
36.35	55	3.67	16.47	26.4	3.78
32.26	51	4.53	13.37	21.2	2.39
27.94	46.0	4.09	11.17	18.0	2.03
24.12	40.3	3.56	9.06	14.6	2.19
20.77	35.6	3.13	7.22	9.9	1.49
18.20	30.8	2.02	Argon (49 mm)		
21.30	40.6	2.94 <sup>a</sup>	75.89	38.3	6.57 <sup>a</sup>
18.81	32.2	2.03	69.31	32.4	6.60
15.73	23.8	2.14	65.68	34.0	3.65
14.31	24.1	2.69	60.60	32.8	3.52
11.87	19.8	2.20	57.09	32.7	3.50
9.74	15.5	2.05	53.59	32.7	3.50
7.99	13.3	1.45	50.15	31.5	3.38
Krypton (23 mm)					
77.19	24.2	3.99 <sup>a</sup>	46.73	32.2	3.45
73.62	21.8	3.15	43.38	32.2	3.45
69.90	20.7	4.28	39.22	30.4	4.89
65.63	20.6	4.26	34.40	29.5	4.74
61.42	20.2	4.17	29.82	27.4	4.41
57.26	20.1	4.14	26.25	25.5	2.73
53.15	19.8	4.08	46.35	37.3	6.39 <sup>a</sup>
49.09	19.6	4.04	40.82	31.3	4.70
47.70	22.5	3.72 <sup>a</sup>	36.79	31.3	3.35
44.44	19.3	2.79	33.54	29.4	3.15
41.10	18.9	3.90	30.54	28.3	3.03
37.10	19.7	4.07	27.52	26.5	2.84
33.18	18.4	3.80	24.75	25.2	2.70
29.47	17.5	3.62	22.14	23.4	2.51
25.97	16.4	3.38	19.75	21.2	2.27
22.68	15.5	3.19	17.14	18.5	2.97
21.37	17.0	2.81 <sup>a</sup>	14.88	15.7	2.53
18.64	13.4	2.63	12.02	13.6	2.19
16.10	11.9	2.46	10.05	10.9	1.76
13.80	10.4	2.14			
11.40	8.6	2.66			
9.06	6.5	2.02			

<sup>a</sup> First segment of gas following the window.<sup>b</sup> Outside experimental error for unknown causes.

TABLE V. Stopping power of iodine ions in gases.

$\bar{E}$ (MeV)	$\Delta E/\Delta X$ (keV cm <sup>2</sup> /μg)	$\Delta E$ (MeV)	$\bar{E}$ (MeV)	$\Delta E/\Delta X$ (keV cm <sup>2</sup> /μg)	$\Delta E$ (MeV)
Hydrogen (240 mm)			Nitrogen (73 mm)		
81.68	413	16.53 <sup>a</sup>	81.54	101	16.92 <sup>a</sup>
70.12	276	6.63	70.41	67	5.24
64.39	257	4.79	64.83	66	5.92
58.95	255	6.09	58.34	63	7.07
52.81	233	6.19	51.61	57	6.37
46.86	217	5.74	45.43	53	5.87
41.47	191	5.05	39.80	49.5	5.53
36.57	180	4.75	34.55	44.5	4.97
31.69	159	5.00	29.79	40.6	4.54
26.88	136	4.63	25.52	35.7	3.99
22.82	110	3.47	21.97	27.9	3.12
19.53	92	3.11	18.83	28.2	3.15
16.43	81	3.05	15.99	22.6	2.53
13.69	64	2.48	13.68	18.8	2.10
Helium (225 mm)			Argon (57 mm)		
85.83	97	8.24 <sup>a</sup>	83.74	67	6.21 <sup>a</sup>
76.58	82	10.28	74.63	46.3	5.79
67.40	83	8.07	68.92	45.1	5.64
60.71	73	5.30	63.36	43.8	5.47
55.51	70	5.10	57.98	42.8	5.34
50.52	67	4.88	52.81	39.8	4.96
45.89	60	4.38	47.86	38.1	4.74
41.56	59	4.29	43.40	35.2	4.38
37.43	55	3.95	39.07	34.4	4.28
34.42	43.3	2.08	34.92	32.4	4.02
43.14	61	5.39 <sup>a</sup>	30.23	28.7	5.35
38.33	56	4.23	25.30	24.2	4.51
33.14	42.1	6.17	21.15	20.4	3.79
27.03	40.7	3.96	41.32	47.1	9.04 <sup>a</sup>
23.38	35.1	3.41	35.16	32.7	3.29
20.22	30.2	2.93	31.62	30.3	3.77
17.47	26.4	2.55	28.56	26.9	2.35
15.11	22.7	2.19	25.60	25.6	3.19
Krypton (220 mm)			Helium (22.7 mm)		
63.64	34.7	52.61 <sup>a</sup>	89.40	118	1.11 <sup>a</sup>
35.32	19.9	4.03	88.34	79	0.99
31.44	18.5	3.74	87.25	81	1.21
26.95	17.3	5.25	85.63	69	2.03
22.22	13.9	4.21	84.00	78	1.13
18.28	12.1	3.66	45.34	106	1.00 <sup>a</sup>
15.00	9.6	2.90	44.45	61	0.77
11.86	8.3	3.38	43.71	48.1	0.72
8.61	6.2	3.12			
29.45	21.6	32.79 <sup>a</sup>			
11.82	8.1	2.45			
10.04	5.6	1.13			
8.09	6.8	2.76			
Krypton (27 mm)					
86.33	39.0	7.24 <sup>a</sup>			
80.92	29.0	3.58			
76.65	26.9	4.97			
71.64	27.4	5.04			
66.75	25.9	4.74			
62.07	25.4	4.63			
57.48	25.0	4.54			
53.06	23.8	4.31			
48.80	23.3	4.20			
44.68	22.5	4.05			
40.73	21.4	3.84			
43.06	30.0	5.57 <sup>a</sup>			
38.98	20.9	2.58			
35.84	20.1	3.71			
32.24	19.0	3.49			
28.90	17.4	3.19			
25.89	15.4	2.82			
23.18	14.3	2.60			
20.71	13.0	2.35			
18.50	11.4	2.06			
16.53	10.4	1.87			
15.74	9.6	1.72			

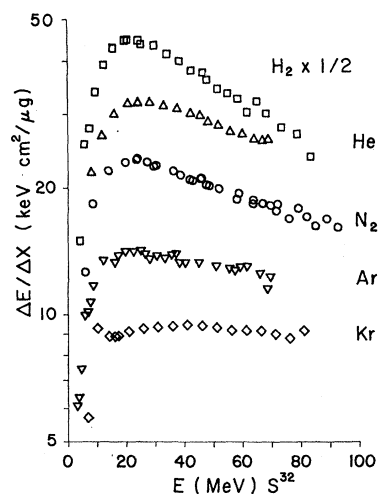
<sup>a</sup> First segment of gas following the window.

FIG. 3. Stopping powers of S<sup>32</sup> ions in H<sub>2</sub>, He, N<sub>2</sub>, Ar, and Kr. The  $\Delta E/\Delta X$  values are plotted versus the mean ion energy through which the energy loss was measured, where the abscissa is the ion kinetic energy. The  $\Delta E/\Delta X$  in H<sub>2</sub> are shown reduced to half their correct values in order to compress the scale for display. Note that the ordinate is a logarithmic scale.

derivatives were taken of these curves, and these in turn were compared with  $\Delta E/\Delta X$ ; the  $dE/dX$  values obtained in this manner showed no consistent differences from  $\Delta E/\Delta X$ , so we will use the experimental  $\Delta E/\Delta X$  values as  $dE/dX$  in subsequent analyses.

#### D. Errors

Errors varied with ion species and, to a degree, with stopping medium. Hydrogen gas, for example, led to rapidly increasing leakage currents for the radiation detectors; the leakage returned to normal after several hours of storage in vacuum. It was thought that this problem may have been due to a small hydrocarbon

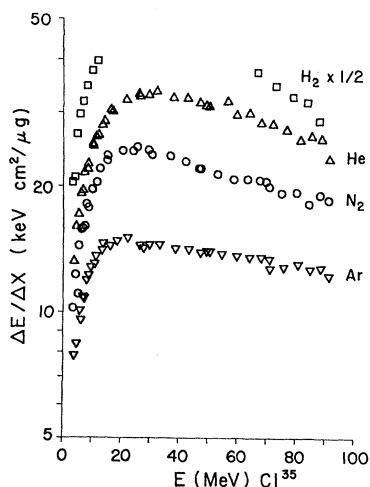


FIG. 4. Stopping powers of Cl<sup>35</sup> ions in H<sub>2</sub>, He, N<sub>2</sub>, and Ar. The comments in the caption of Fig. 3 are applicable to this figure as well. Note that stopping powers in H<sub>2</sub> were not measured over the entire range as is discussed in the text.

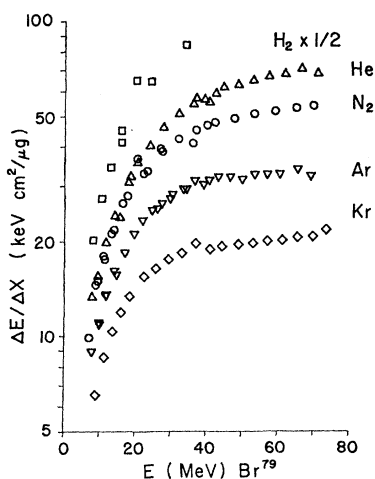


FIG. 5. Stopping powers of  $\text{Br}^{79}$  in  $\text{H}_2$ , He,  $\text{N}_2$ , Ar, and Kr. The comments in the caption of Fig. 3 are applicable to Fig. 5.

impurity in the 99.9% pure  $\text{H}_2$  gas supply. Considering all sources of errors, which have been individually discussed in earlier sections, we estimate average errors in  $\Delta E/\Delta X$  of 3% for S ions and Cl ions, 4% for Br ions, and 5% for I ions. It is possible that because of the rapidly changing detector leakage currents for measurements in  $\text{H}_2$  these data have slightly greater errors, although spectral responses give no cause to suspect this. It was because of this leakage problem that we report only partial results for  $\text{Cl}^{35}$  ions in  $\text{H}_2$ ; the measurements were not continued after leakage currents reached given levels.

### III. RESULTS AND DISCUSSION

#### A. Data Correlation

In this subsection, we attempt a semiempirical correlation of the gas stopping data presented in the

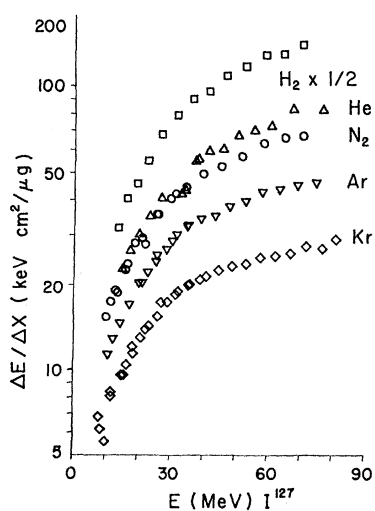


FIG. 6. Stopping powers of  $\text{I}^{127}$  in  $\text{H}_2$ , He,  $\text{N}_2$ , Ar and Kr. The comments in the caption of Fig. 3 apply to this figure as well.

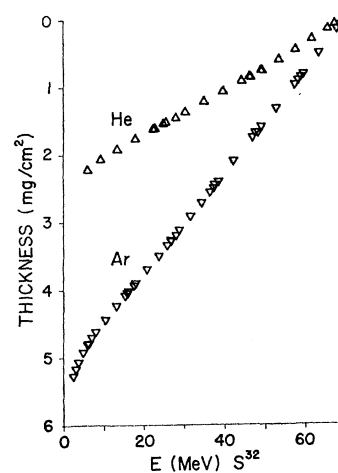


FIG. 7. Thickness versus energy curves for  $\text{S}^{32}$  ions in He and Ar. The ordinate is arbitrarily taken as zero for an initial ion energy of 69 MeV. The energy of the beam is then shown on the abscissa as a function of the gas thickness (on the ordinate) through which the beam has passed. The abscissa represents  $\text{S}^{32}$  ion kinetic energy.

previous section in order to provide a means of interpolation and extrapolation to as yet unmeasured ion-gas stopper combinations. We next will apply the same treatment to available solid stopping data and compare these results with those for gas stopping. This should provide a quantitative measure of the importance of state of condensation of stopping medium on  $\Delta E/\Delta X$ . The general procedure to be followed has been used by many groups<sup>7-12</sup> in the past for the purpose of corre-

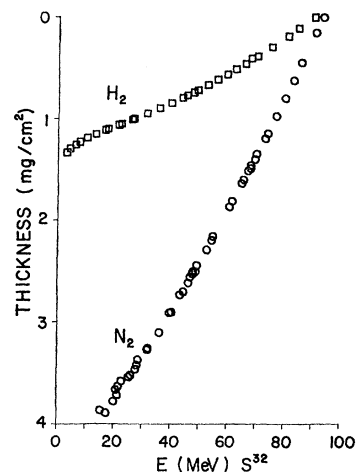


FIG. 8. Thickness-versus-energy curves for  $\text{S}^{32}$  ions in  $\text{H}_2$  and  $\text{N}_2$ . The comments in the caption of Fig. 7 are relevant to Fig. 8, but the initial  $\text{S}^{32}$  ion energy is 92 MeV.

<sup>7</sup> W. H. Barkas, *Nuclear Research Emulsions* (Academic Press Inc., New York, 1963), Vol. I.

<sup>8</sup> H. H. Heckman, E. L. Hubbard, and W. G. Simon, *Phys. Rev.* **129**, 1240 (1963).

<sup>9</sup> H. H. Heckman, B. L. Perkins, W. G. Simon, F. M. Smith, and W. H. Barkas, *Phys. Rev.* **117**, 544 (1960).

<sup>10</sup> W. Booth and I. S. Grant, *Nucl. Phys.* **63**, 481 (1965).

<sup>11</sup> P. G. Roll and F. E. Steigert, *Nucl. Phys.* **16**, 534 (1960); **17**, 54 (1960); *Phys. Rev.* **120**, 470 (1960).

<sup>12</sup> L. C. Northcliffe, *Ann. Rev. Nucl. Sci.* **13**, 67 (1963).

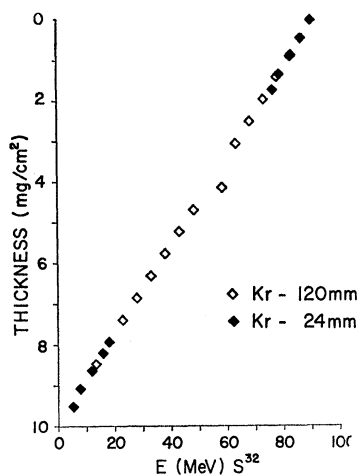


FIG. 9. Thickness-versus-energy curves for  $S^{32}$  ions in Kr. Two pressures of Kr were used in these measurements, as is discussed in the text. Definitions of the significance of the axes of this figure are as in the caption of Fig. 7. Zero thickness is at 92 MeV.

lating heavy-ion stopping data and was suggested by Bohr and Lindhard.<sup>13,14</sup>

The data are to be correlated making use of the functional dependences of the Bethe<sup>6</sup> stopping-power equation

$$(dE/dX)_{Z,A,E} \propto Z^2 (Z_2/A_2 v^2) \ln(2mv^2/I), \quad (1)$$

where the electronic stopping power  $(dE/dX)_{Z,A,E}$  of an ion of atomic number  $Z$ , mass number  $A$ , and kinetic energy  $E$  is proportional to the square of the nuclear charge of the beam particles  $Z^2$ , the nuclear charge of the stopping medium  $Z_2$ , its mass number  $A_2$ , plus

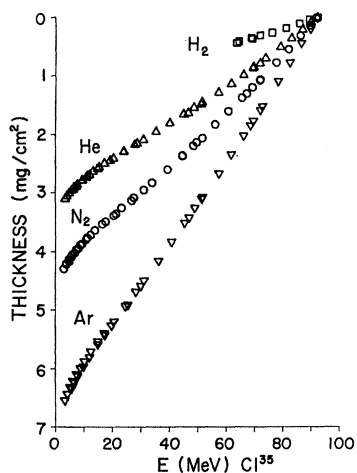


FIG. 10. Thickness-versus-energy curves for  $Cl^{36}$  ions in  $H_2$ , He,  $N_2$ , and Ar. Zero thickness is at  $\sim 92$  MeV. Ordinate and abscissa axes are defined as in the caption of Fig. 7.

<sup>13</sup> N. Bohr and J. Lindhard, Kgl. Danske Videnskab. Selskab, Mat. Fys. Medd. **28**, No. 7 (1954).

<sup>14</sup> J. Lindhard, M. Scharff, and H. E. Schiott, Kgl. Danske Videnskab. Selskab, Mat. Fys. Medd. **33**, No. 14 (1963). The Eq. (3) is from J. Lindhard (private communication).

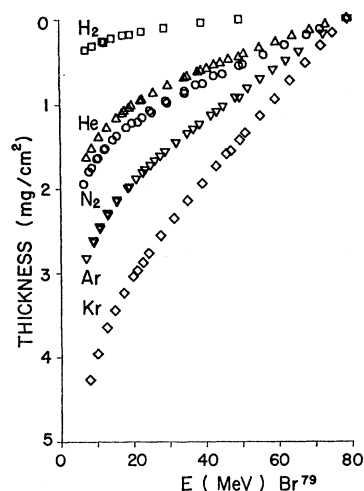


FIG. 11. Thickness-versus-energy curves for  $Br^{79}$  ions in  $H_2$ , He,  $N_2$ , Ar, and Kr. Zero thickness is at  $\sim 76$  MeV for all ions except  $H_2$ , which begins at  $\sim 49$  MeV. Ordinate and abscissa axes are as defined in the caption of Fig. 7.

factors which are a function solely of the ion velocity and stopping medium. The restrictions which went into the derivation of the Bethe equation make its literal application to the present systems totally inappropriate. One obvious reason is that the actual charges carried on the ions under discussion are only a fraction of their nuclear charge. This suggests replacement of the nuclear charge in Eq. (1) by an effective charge,  $Z_{\text{eff}} = \gamma Z$ . Replacement of  $Z$  by the rms charge in Eq. (1) still may not give a valid theory for heavy-ion energy losses since all restrictions in the derivation may not be satisfied. Nonetheless, we use Eq. (1) as a starting point to seek a smooth function relating the effective charge to the ion velocity, where the relationship of effective charge to rms charge is not at all clear and the effective charge is to be considered simply as a

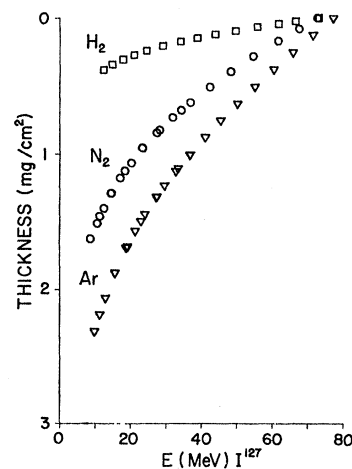


FIG. 12. Thickness-versus-energy curves for  $I^{127}$  ions in  $H_2$ ,  $N_2$ , and Ar. Zero thickness is taken as  $\sim 75$  MeV. Ordinate and abscissa axes are as defined in the caption of Fig. 7.

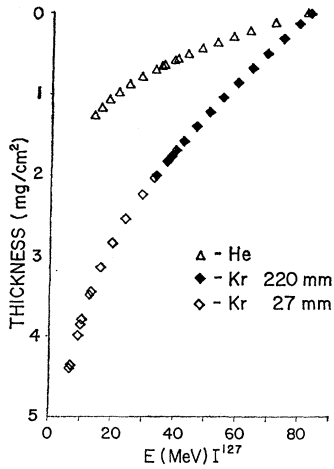


FIG. 13. Thickness-versus-energy curves for  $I^{127}$  ions in He and Kr. Two pressures of Kr were used, as is discussed in the text. Zero thickness was taken as  $\sim 80$  MeV. The ordinate and abscissa are as defined in the caption of Fig. 7.

parameter. To do this, we consider the relationship of Eq. (1) for a given velocity heavy ion to that of a proton of the same velocity in the same stopping medium. If, in fact, the assumption that all but the  $Z^2$  terms are a function of velocity and stopping medium is correct, then

$$\frac{(dE/dX)_{Z,A,E}}{(dE/dX)_{p,E/A}} = \frac{\gamma^2 Z^2 (Z_2/A_2 v^2) \ln(2mv^2/I)}{\gamma_p^2 (Z_2/A_2 v^2) \ln(2mv^2/I)} = \frac{\gamma^2 Z^2}{\gamma_p^2}, \quad (2)$$

where  $\gamma_p$  is the fraction of time the proton has unit charge, other symbols having the significance stated in the discussion following Eq. (1), the denominator on the left of Eq. (2) representing the electronic stopping power of a proton of kinetic energy  $E/A$  in a medium  $Z_2, A_2$ . Thus, by inserting the measured heavy-ion stopping powers of this work with published proton stopping powers into Eq. (2), the effective charge of the heavy ion may be calculated as a function of velocity. Over most of the velocity range covered in this work,  $\gamma_p^2$  was essentially unity. Where this was not the case, values of  $\gamma_p^2$  due to Hall, as reported by Booth and Grant,<sup>10</sup> were used in calculating  $\gamma Z$ .

In order to compare different ionic species on the same basis, the effective charges are converted to fractional effective charges ( $Z_{\text{eff}}/Z = \gamma$ ), and the velocities are converted to reduced velocities prior to comparison. The reduced velocity used in this work is the ratio of ion velocity to the Thomas-Fermi electron velocity  $v/(v_0 Z^{2/3})$ , where  $v_0 = e^2/\hbar$ . A nomogram for computing reduced velocities is presented in the Appendix. Corrections for nuclear stopping of up to 24% were made to the stopping powers listed in Tables II-V prior to calculating effective charges, since the form of Eq. (1) is for electronic stopping only. The

asymptotic formula used was

$$(d\epsilon/d\rho)_n = (1/2\epsilon) \ln 1.294\epsilon, \quad \epsilon \geq 10 \quad (3)$$

where  $\rho$  and  $\epsilon$  are the dimensionless range and energy variables defined by Lindhard *et al.* and where the subscript  $n$  denotes nuclear stopping.<sup>14</sup> The maximum corrections applied to each ion, as well as the ion energy at which the correction was 1%, are summarized in Table VI.

The correlations of fractional effective charge versus reduced velocity are shown for different ions in each stopping medium of this work in Figs. 14-18; the correlation against a single smooth curve is well within experimental errors, with the possible exception of the effective charges of  $I^{127}$  ions in hydrogen (Fig. 14). The same anomaly was observed for  $Ar^{40}$  ions in  $H_2$  by Martin and Northcliffe,<sup>15</sup> who offer an explanation in terms of the theory of Bohr and Lindhard.<sup>13</sup> The basis of the explanation lies in the low binding energy of the hydrogen electron relative to the average binding energy in heavier elements. This leads to the situation of ionization of hydrogen at such large ion-molecule distances that the electron is not available for capture by the ion so that the electron capture-to-loss ratio for the ions in hydrogen is considerably below the value for

TABLE VI. Percent nuclear stopping contributions estimated for measured  $\Delta E/\Delta X$ .

Ion	Stopping media	$E$ lowest <sup>a</sup> (MeV)	% at $E$ lowest <sup>b</sup>	Energy <sup>c</sup> at 1% (MeV)
$S^{32}$	Ar	2.90	3.1	6
	He	7.87	0.5	6
	$N_2$	5.69	1.2	6
	$H_2$	3.89	2.7	7
	Kr	6.73	1.4	8
$Cl^{35}$	Ar	3.86	2.3	7
	He	3.98	2.0	7
	$N_2$	3.53	2.6	7
	$H_2$	3.44	2.1	7
$Br^{79}$	Ar	7.94	8.2	30
	He	7.99	7.8	25
	$N_2$	7.22	12.0	27
	$H_2$	8.21	8.2	27
	Kr	9.06	6.3	40
$I^{127}$	Ar	10.65	15.0	65
	He	15.11	7.8	55
	$N_2$	10.11	15.0	65
	$H_2$	13.69	10.0	45
	Kr	8.09	24.0	>80

<sup>a</sup> Lowest energy for which stopping powers were measured for the ion and stopping medium indicated.

<sup>b</sup> Percent nuclear stopping correction calculated for the lowest beam energy.

<sup>c</sup> This column lists the energy above which the estimated nuclear stopping contribution is less than 1% of the measured stopping power.

<sup>15</sup> F. W. Martin and L. C. Northcliffe, *Phys. Rev.* **128**, 1166 (1962).

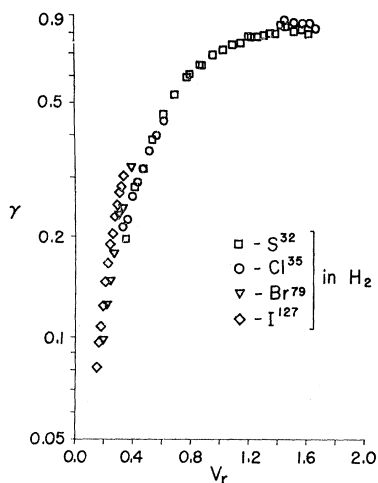


FIG. 14. Correlation of fractional effective charge  $\gamma$  versus the reduced velocity  $v_r$  for heavy ions in  $H_2$ . The parameters  $\gamma$  and  $v_r$  are defined in the text.

higher- $Z$  media. Because the points of Figs. 14-18 define their own curve quite satisfactorily, a solid line has not been drawn. Not all the points of Tables II-V were put on Figs. 14-18 for reasons of space; those which were omitted fall on the loci of plotted points, with the exception of those omitted for cause as discussed in Sec. II.

The effective charge curves of Figs. 14-18 are compared with each other in Fig. 19, where for clarity only the smooth solid curves corresponding to the loci of points in Figs. 14-18 are shown. The agreement for all ions in all gases except hydrogen is well within the experimental uncertainties of the experimental heavy-ion and proton stopping powers. Since the proton data were interpolated from small published graphs on a log-log scale, there is a  $\pm 5\%$  uncertainty, due to the

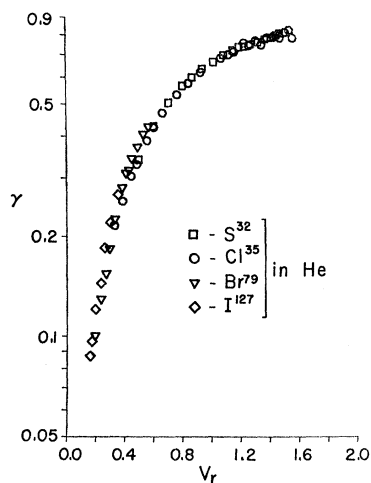


FIG. 15. Correlation of fractional effective charge versus reduced velocity for heavy ions in He.

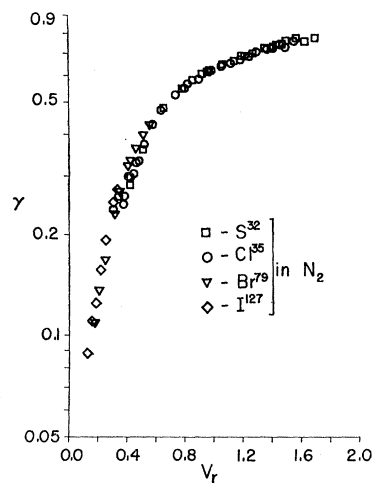


FIG. 16. Correlation of fractional effective charge versus reduced velocity for heavy ions in  $N_2$ .

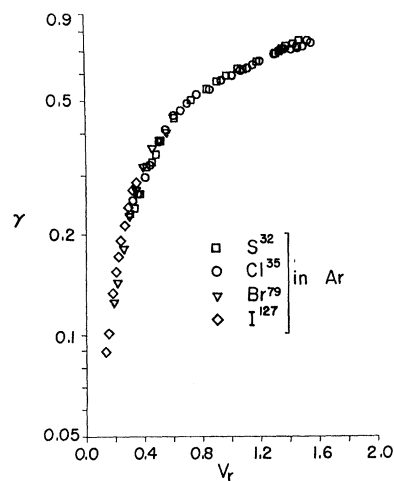


FIG. 17. Correlation of fractional effective charge versus reduced velocity for heavy ions in Ar.

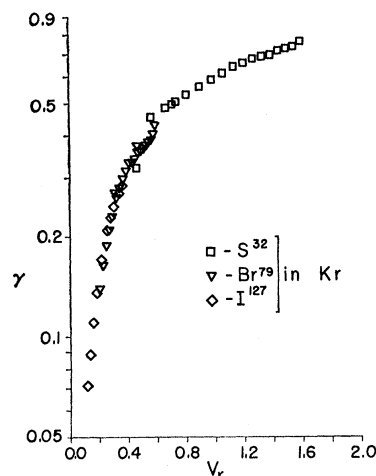


FIG. 18. Correlation of fractional effective charge versus reduced velocity for heavy ions in Kr.

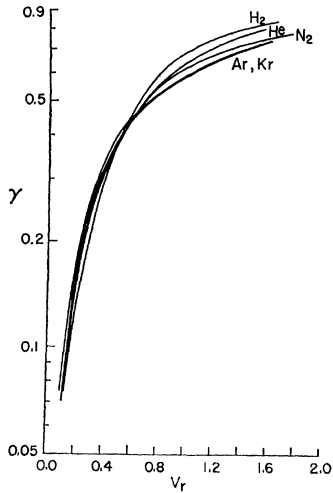


FIG. 19. Comparison of fractional effective charge versus reduced velocity curves for the five stopping media investigated in this work. The solid curves represent the best curves drawn visually through the points of Figs. 14-18.

interpolation alone.<sup>16</sup> The experimental uncertainties of the proton stopping data are of the order of  $\pm 1-5\%$ . Since the effective charges for stopping in hydrogen are 10% greater than the median for the other gases, it is not obvious that the charges in hydrogen are anomalously high, but this may very well be the case.

Stopping powers in Be, C, Al, Ni, Ag, and Au, for  $O^{16}$ ,  $Cl^{35}$ ,  $Br^{79}$ , and  $I^{127}$  ions have been analyzed in terms of effective charge and the results are presented in Figs. 20-25. The  $O^{16}$  and  $Cl^{35}$  data are those of Booth and Grant<sup>10</sup>;  $Br^{79}$  and  $I^{127}$  data are those of Moak and Brown.<sup>17</sup> As with gas stopping data, fractional effective

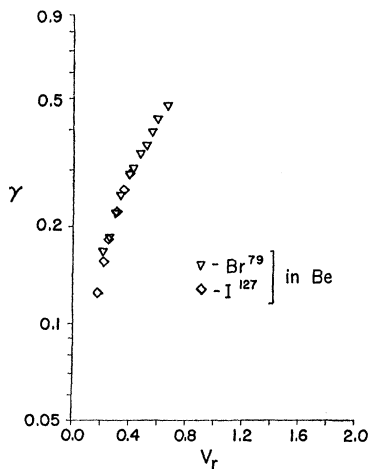


FIG. 20. Correlation of fractional effective charge versus reduced velocity for heavy ions in Be. The stopping powers used were from Ref. 17.

<sup>16</sup> W. Whaling, *Encyclopedia of Physics*, edited by S. Flügge (Springer-Verlag, Berlin, 1958), Vol. 34, p. 193.

<sup>17</sup> C. D. Moak and M. D. Brown, *Phys. Rev.* **149**, 244 (1966).

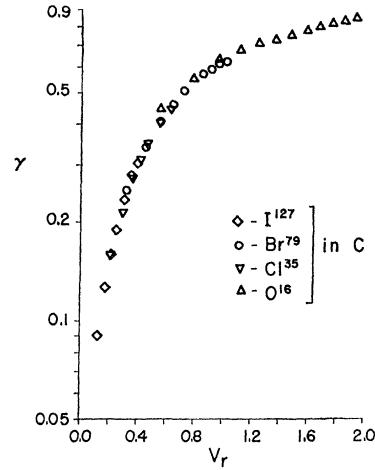


FIG. 21. Correlation of fractional effective charge  $\gamma$  versus reduced velocity  $v_r$  for heavy ions in C. The stopping powers used were from Refs. 10 and 17.

charges for heavy ions in solids lie on single smooth curves within a given material. The experimental uncertainties of the solid stopping data are 5 to 10%.

The relationship between effective charge curves for solid and gas stopping media is illustrated in Fig. 26, where the maximum and minimum loci of points from Figs. 14-18 and 20-25 are shown as the upper and lower solid curves, respectively. The effective charges for hydrogen are not shown in Fig. 26; the relationship of the hydrogen values to other effective charges may be seen by reference to Fig. 19. It may be seen in Fig. 26 that within the experimental uncertainties there is no difference in effective charge and, therefore, in stopping power between solids and gases (since the proton stopping powers show no state of condensation dependence). The dashed curve of Fig. 26 is the

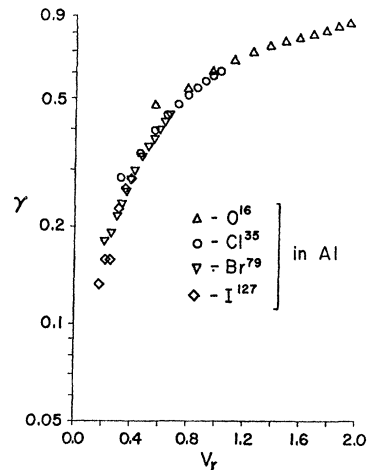


FIG. 22.  $\gamma$  versus  $v_r$  for heavy ions in Al. Stopping powers used were from Refs. 10 and 17.

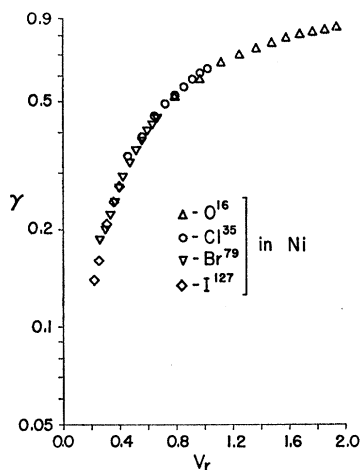


FIG. 23.  $\gamma$  versus  $v_r$  for heavy ions in Ni. Stopping powers used were from Refs. 10 and 17.

analytic expression

$$\gamma = 1 - \exp(-125\beta/Z^{2/3}), \quad (4)$$

which was presented by Barkas<sup>7</sup> to fit stopping-power data of Heckman<sup>8</sup> *et al.* for heavy ions such as C, N, and O, as well as some fission-fragment data. The deviation from our curve at low velocities may be due to our subtraction of a nuclear stopping contribution from the total stopping power prior to calculating  $\gamma$ .

The data of this work, supplemented by stopping powers of lighter heavy ions<sup>12</sup> in the region  $v_r \geq 2$ , and with Sikkeland's data<sup>18</sup> for Ar<sup>40</sup> in Al ( $1 \leq v_r \leq 3$ ), are better fit by the analytic expression

$$\gamma = 1 - \exp(-0.95v_r), \quad (5)$$

where  $v_r$  is the previously defined reduced velocity. The additional data were used to check Eq. (5) beyond the upper limit of  $\gamma$ , 0.85, of this work, allowing its extension

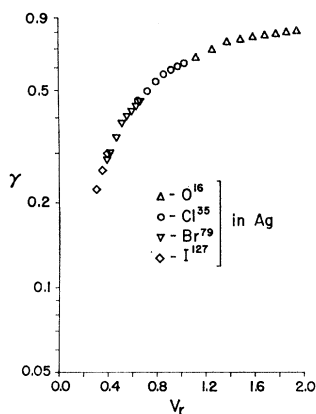


FIG. 24.  $\gamma$  versus  $v_r$  for heavy ions in Ag. Stopping powers used were from Refs. 10 and 17.

<sup>18</sup> T. Sikkeland, University of California Radiation Laboratory Report No. UCRL-16453, 1965 (unpublished).

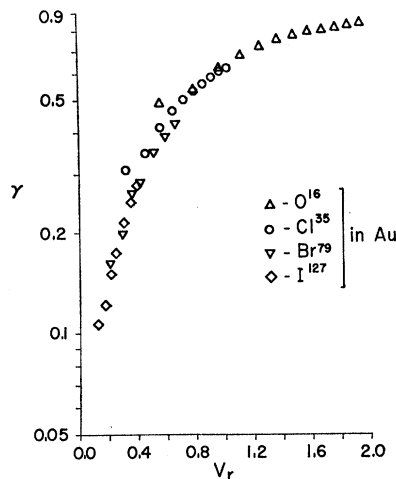


FIG. 25.  $\gamma$  versus  $v_r$  for heavy ions in Au. Stopping powers used were from Refs. 10 and 17.

to  $\gamma \approx 1$ . For reduced velocities beyond those for which heavy-ion stopping-power data are available ( $v_r \approx 5$ ), ions should be fully stripped; and the Bethe-Block stopping theory should be valid. Below the region covered by Fig. 26, the stopping theory of Lindhard, Scharff, and Schiott<sup>14</sup> (LSS) has been shown to be valid.<sup>19-21</sup> Over the velocity region above which the LSS stopping theory is valid, i.e., above  $v_r \approx 0.1$ , the following semiempirical stopping equation may be used:

$$\left(\frac{dE}{dX}\right)_{Z,A,E} = \left(\frac{dE}{dX}\right)_{v,E/A} \times Z^2 [1 - \exp(-0.95v_r)]^2 [1 - \exp(-2.5v_p)]^{-2}, \quad (6)$$

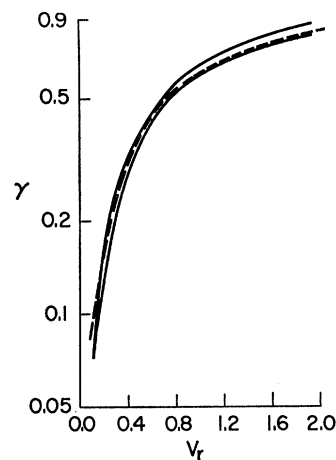


FIG. 26. Comparison of  $\gamma$  versus  $v_r$  correlations for heavy ions in He, Ne, Ar, Kr, Be, C, Al, Ni, Ag, and Au. The two solid lines represent the upper and lower limits of the smooth curves drawn through the points in Figs. 15-18 and 20-25. The dashed curve is the analytic expression of Eq. (4) due to Barkas, Ref. 7.

<sup>19</sup> J. M. Alexander, in *Nuclear Chemistry*, edited by L. Yaffe (Academic Press Inc., New York, 1968), Chap. 4, p. 273.

<sup>20</sup> W. W. Bowman, F. M. Lanzafame, C. K. Cline, Yu-Wen Yu, and M. Blann, *Phys. Rev.* **165**, 485 (1968).

<sup>21</sup> J. M. Alexander and L. Winsberg, *Phys. Rev.* **121**, 529 (1961).

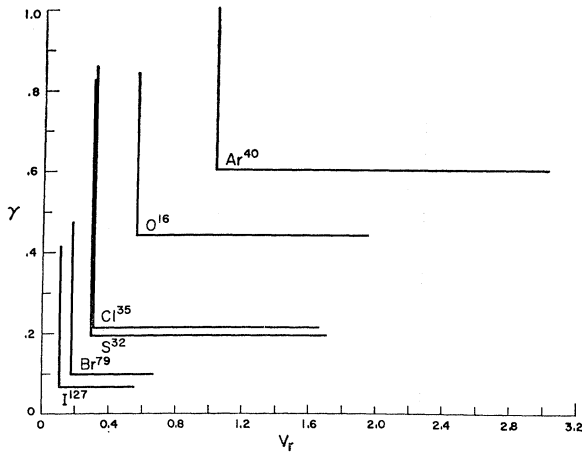


FIG. 27. Overlap in  $\gamma$  and  $v_r$  for heavy ions. The lines on ordinate and abscissa represent the span in  $\gamma$  and  $v_r$ , respectively, over which we have correlated heavy-ion stopping powers. The  $\text{Ar}^{40}$  data from Ref. 18 have not been shown explicitly on any of the figures but are in agreement with the correlation curve found. Stopping powers for  $\text{O}^{16}$  from Ref. 12 may be used to extend the curve of Fig. 26 up to  $v_r \approx 5$ .

where the term on the left represents the electronic stopping power for a heavy ion of atomic number  $Z$ , mass number  $A$ , and kinetic energy  $E$ ; the first factor on the right represents the experimental or calculated proton stopping power of a proton of kinetic energy  $E/A$ , the second factor represents the square of the heavy-ion atomic number, the third factor is  $\gamma^2$  from Eq. (5), and the final term gives an analytic fit to the rms charge term for protons at low velocities. In the latter expression the constant has units  $\text{MeV}^{-1/2}$ , where the proton velocity  $v_p$  is to be used in units of  $\text{MeV}^{1/2}$ . This last ( $\gamma v_p^{-2}$ ) factor is essential only in the velocity region corresponding to proton energies below

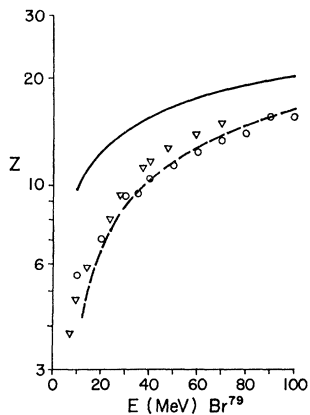


FIG. 28. Effective charges for  $\text{Br}^{79}$  ions in gas and solid stopping media versus the equilibrium rms charges in gas and solid strippers. The solid curve represents the equilibrium rms charge versus energy for  $\text{Br}$  ions in  $\text{C}$  foils; the dashed curve represents the equilibrium rms charge versus energy for  $\text{Br}$  ions in  $\text{Ar}$ . The open inverted triangles represent effective charges  $\gamma Z$  for  $\text{Br}$  ions in  $\text{Ar}$  and  $\text{N}_2$ ; and the open circles represent effective charges for  $\text{Br}^{79}$  ions in  $\text{C}$ .

0.3 MeV, i.e., heavy-ion velocities under 0.3 MeV/amu. Above this energy, Eq. (6) may be written in the simpler form

$$(dE/dX)_{Z,A,E} = (dE/dX)_{p,E/A} Z^2 [1 - \exp(-0.95v_r)]^2, \quad E/A \geq 0.3 \text{ MeV}. \quad (7)$$

If the correlations indicated in Fig. 26 are valid, electronic stopping powers calculated in this manner should be accurate to  $\pm 8\%$  or better. In the lower velocity regions (see Table VI), a nuclear stopping contribution should be added to the electronic stopping power to get the total stopping power. The asymptotic equation due to Lindhard,<sup>14</sup> Eq. (3), should be useful in this respect.

While Fig. 26 seems to present a convincing case for a universal curve of fractional effective charge versus

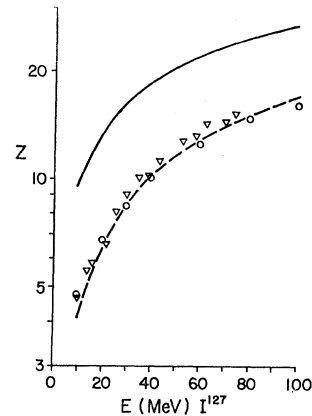


FIG. 29. Effective charges for  $\text{I}^{127}$  ions in gas and solid stopping media versus the equilibrium rms charges in gas and solid strippers. The solid curve represents the equilibrium rms charge versus energy for  $\text{I}^{127}$  ions in  $\text{C}$  foils; the dashed curve represents the equilibrium rms charge versus energy for  $\text{I}^{127}$  ions in  $\text{Ar}$ . The open inverted triangles represent effective charges  $\gamma Z$  for  $\text{I}^{127}$  ions in  $\text{Ar}$  and  $\text{N}_2$ ; and the open circles represent effective charges for  $\text{I}^{127}$  ions in  $\text{C}$ .

reduced velocity, at the same time indicating the usefulness of the Thomas-Fermi approach in this field, it should be emphasized that all the beam species considered do not span the entire range of the curve. The degree of overlap may be seen in Fig. 27. It would be desirable to extend the measurements to considerably higher energies for ions such as  $\text{Br}^{79}$  and  $\text{I}^{127}$ , as well as looking at considerably higher mass ion beams such as  $\text{U}^{238}$ ; size effects may very well cause deviations from the correlations found for lighter ions. These reservations must be kept in mind when using Eq. (6) as an extrapolation formula.

## B. Relationship of Effective Charge to rms Charge

The most probable charges for  $\text{Br}^{79}$  and  $\text{I}^{127}$  ion beams are shown versus the effective charges in gases and in solids in Figs. 28 and 29. The most probable charge does not differ by more than a few tenths of a unit charge

from the rms charge. There is evidence that the equilibrium charge states are a function mainly of ion velocity, with at best a weak dependence on stripping medium in a given state.<sup>4</sup> For gas stopping, the effective charges are quite close to the reported most probable or rms charge values<sup>2-4</sup>; they are in agreement to within the uncertainties due to experimental errors and screening effects. The same comparison is made for some of the solid stopping media in the same figures. There is a dramatic difference between effective and most probable charge states in solids, especially in the case of I<sup>127</sup> beams. The comparisons are not shown for S<sup>32</sup> and Cl<sup>35</sup> beams because the differences between rms charges in gases and solids do not differ greatly for these ions. Thus, we find that solids and gases show no stopping-power dependence on state of condensation within the limits of experimental uncertainties of this and related work. Yet, while the effective and most probable charges are in reasonable agreement for gases, they bear no obvious relationship in solids. We would emphasize this point with the thought that, while use of rms charges with Eq. (1) will yield reasonable calculated stopping powers for gases, they may give values in error by nearly a factor of 4 for solids.

One possible explanation of the apparent charge state discrepancy in solids has been suggested by Bennemann.<sup>22</sup> The ions in penetrating solid media are in a potential well with respect to penetration of a gas; this may be thought of as being due to the work function differences between solids and gases or equivalently to the high electron density seen by the ion in a closely packed solid. Thus, many multiply excited electrons which would be lost in a stripping process are still bound within the solid because of the potential difference caused by high electron density. As the ion emerges from the solid, the potential changes; and these electrons are trapped in the solid. Thus, the effective charge reflects no significant difference in gases and solids since there is none. The ion carries the same charge during the stopping process in both media. The measured rms charges differ because the heavy-ion charge is measured not in the solid, but after leaving it. The proton stopping powers<sup>16</sup> show no significant deviation from a smooth trend between gas and solid stopping media, and this would rule out polarization effects as an explanation of this apparent stopping-power anomaly. We present this as one reasonable interpretation of the data; it is not unique and it is speculative.

A set of measurements was made to look qualitatively at the effect of true charge state on stopping powers in gases. Since the equilibrium charge states of ions passing through the Mylar window are higher than the equilibrium values in gases, the ions enter the gas cell with higher than their equilibrium charges. Thus, if the ionic charge determines the stopping power, higher

<sup>22</sup> K. H. Bennemann (private communication).

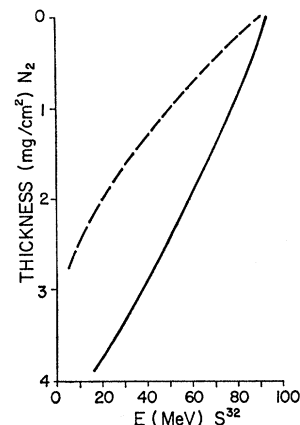


FIG. 30. Comparison of experimental thickness versus energy curve for S<sup>32</sup> ions in N<sub>2</sub> with the values predicted by the LSS range theory. The solid curve represents the experimental result; the dashed curve represents the theoretical prediction.

$dE/dX$  values would be expected for path lengths less than the thickness for charge equilibration. The pressure in the cell was reduced to 23 mm for He gas, allowing measurements of  $dE/dX$  for which a considerable portion of the ion path length was less than the equilibrium thickness. The results of these measurements for I<sup>127</sup> ions are summarized in Table V. As expected, there is a large increase in  $dE/dX$  for the first unit of path length, and the increase is outside the errors to be expected owing to uncertainty in the window-to-detector distance. At these low pressures, it is unlikely that the increase in the measured  $\Delta E$  is due to bowing of the Mylar window causing an increased energy loss in the window. Those data of Tables II-V corresponding to the  $\Delta E/\Delta X$  obtained for the first region of the gas cell generally show high values, and this may be due to the same charge-state effect. Since the effect seems greater for Br<sup>79</sup> and I<sup>127</sup> ions than for S<sup>32</sup> and Cl<sup>35</sup> ions and since the solid versus gas rms charge differences are greater for the former two ions than for the latter two, this seems a reasonable but at present purely speculative explanation.

### C. Dependence of Stopping Powers on Gas Pressure

In Figs. 9 and 13, energy-loss data are plotted in terms of ranges for  $\Delta E/\Delta X$  values measured with gas pressures varying by up to a factor of 8. These data show no deviation as a function of pressure within the experimental uncertainties. We conclude that the stopping powers measured are independent of pressure, at least over the fairly broad range included in this work. While this result was expected, it could not have been concluded *a priori*.

### D. Comparison of LSS Ranges and Experimental Ranges

A few of the experimental energy-versus-thickness curves are compared with values predicted by the LSS theory<sup>14</sup> in Figs. 30-32. It may be seen that some values predicted are high, while others are low, with errors approaching a factor of 2.

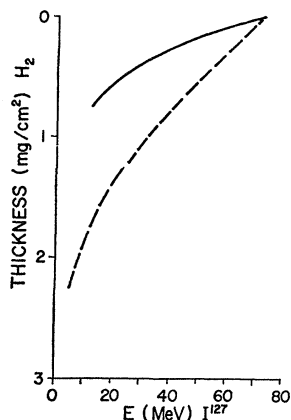


FIG. 31. Comparison of experimental thickness versus energy curve for  $I^{127}$  ions in  $H_2$  with the values predicted by the LSS range theory. The solid curve represents the experimental results; the dashed curve represents the theoretical prediction.

#### IV. CONCLUSIONS

Heavy-ion stopping powers may be correlated for both solid and gaseous stopping media by using the concept of fractional effective charge and reduced velocity. For the latter parameter, a Thomas-Fermi atomic model proves to be entirely adequate. Stopping powers for all media He through Au for incident ions  $O^{16}$  through  $I^{127}$  yield a single smooth curve on this basis, where all points fall on the curve to within the experimental uncertainties, although data for different heavy ions do not overlap the entire range of the effective charge curve presented. The latter values (experimental stopping powers and resulting effective charges) are accurate to the order of  $\pm 5\%$  or better. The correlation for stopping powers in hydrogen is on the borderline of being in agreement to within the experimental uncertainties. There is no evidence for differences in stopping powers due to state of condensation of the medium; the evidence, in fact, is that there is no difference between solids and gases in this respect. Stopping powers for a wide range of ions and stopping media may well be calculable using the effective-charge-versus-reduced-velocity curve, proton stopping powers, and the functional form of the Bethe stopping-power theory, or the analytic expression pro-

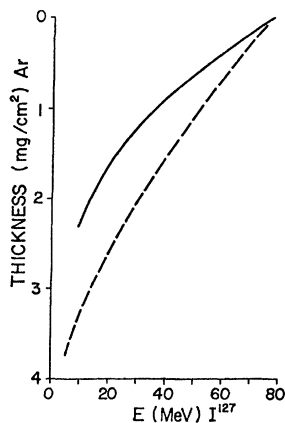


FIG. 32. Comparison of experimental thickness-versus-energy curves for  $I^{127}$  ions in Ar, with the values predicted by the LSS range theory. The solid curve represents the experimental results; the dashed curve represents the theoretical prediction.

vided in the preceding section of this report. This curve extends from a low-velocity region, where the LSS stopping theory is valid, to a high-velocity region, where the ions are fully stripped and where the Bethe stopping theory should apply, i.e.,  $0.1 \leq v_r \leq 5$ . Over the velocity region covered in this work, neither the range theory of LSS nor the stopping equation of Bethe is adequate. For gas stopping, the effective charges agree with the rms charges determined in independent charge-state measurements; whereas for solid stopping media, discrepancies of as much as 70% exist between rms and effective charge states. A possible explanation for this discrepancy is based on the different potentials seen by the ion beams in gases and solids. The true ionic charge may be the same in both media, as perhaps

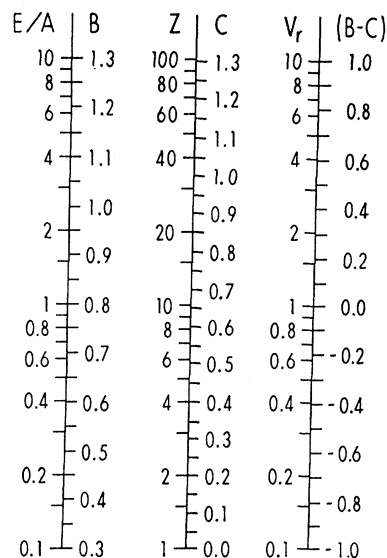


FIG. 33. Nomogram for relating kinetic energy  $E$  (MeV), mass number  $A$ , and atomic number  $Z$  to the reduced velocity variable  $V_r$ , used in this work. Use of the nomogram is described in the Appendix.

the analysis in terms of effective charge suggests, with extra electrons being stripped as the ions leave the solid stopping media.

#### ACKNOWLEDGMENTS

We gratefully acknowledge the support of the Nuclear Structure Laboratory, which is supported by the National Science Foundation, for providing the accelerator time for this work. We acknowledge helpful discussions with and suggestions from Dr. P. B. Price, Dr. K. H. Purser, and A. N. Petersen. The help of Dr. W. W. Bowman in performing these experiments is also sincerely appreciated. The support of the entire staff of the Nuclear Structure Laboratory was indispensable, with special thanks due to R. A. Hawrylak for aid in the mechanical design of the experimental

apparatus. We also very much appreciated helpful discussions with and suggestions from Dr. J. B. Cumming, who called our attention to the method used in correlating the data of this work.

#### APPENDIX

Since the relationship between energy and reduced velocity,  $V_r$ , is one which requires considerable arithmetic, we have prepared Fig. 33 to permit ready conversions between these variables. Three double scales

are presented in Fig. 33; in each case the left-hand side is logarithmic, while the right-hand side is linear. To calculate  $V_r$  for an ion of kinetic energy  $E$  (MeV), atomic number  $Z$ , and mass number  $A$ , find the MeV/nucleon value under the  $E/A$  scale of Fig. 33, and read the value of  $B$ . Next find the atomic number on the scale marked  $Z$ , and read the corresponding number  $C$ .

Finally read the value of  $V_r$  on the third log scale opposite the difference  $(B-C)$  on the linear scale.

## Radiationless Annihilation of Positrons in Lead

SAKAE SHIMIZU, TAKESHI MUKOYAMA, AND YASUYUKI NAKAYAMA

*Institute for Chemical Research, Kyoto University, Kyoto, Japan*

(Received 23 October 1967; revised manuscript received 20 May 1968)

A process of positron annihilation without emission of radiation, *radiationless* or *zero-quantum annihilation*, has been investigated experimentally. A theory for this phenomenon has also been developed. The 300-keV positrons were focused on a thin lead target by the use of a Siegbahn-Slätis intermediate-image spectrometer mounted with  $\text{Na}^{22}$  as a positron source. The shell electrons ejected from the lead foil were observed with a lithium-drifted silicon detector mounted immediately behind the foil. We have observed a small peak in the expected energy region of the electron spectrum. This has been attributed to the shell electrons ejected from the lead foil. The effect of target thickness has been examined carefully as an important factor influencing our observations. Using the experimental data obtained, we have attempted to estimate the total cross section of this annihilation process in lead. Our experimental result is  $\sigma_{\text{exptl}} = 0.8_{-0.8}^{+0.4} \times 10^{-26} \text{ cm}^2$  as a sum of those for  $K$ - $K$ ,  $K$ - $L$ ,  $K$ - $M$ , and  $L$ - $L$  pairs of shell electrons in a lead atom for 300-keV positrons. The calculated cross section we obtained is  $\sigma_{\text{calc}} = 0.727 \times 10^{-26} \text{ cm}^2$ . Our experimental value is in agreement with the calculated result within the experimental error. The present work has established the experimental evidence for this mode of positron annihilation, and has furthered understanding of the process.

### 1. INTRODUCTION

IT is well known that when a positron annihilates in collision with an electron there exist two distinct processes, i.e., annihilation by a free electron and by an electron strongly bound in an atom. In the former case, at least two photons are emitted because of the conservation law of momentum, while in the latter only a single-quantum annihilation can take place. Many theoretical and experimental works on these two types of the annihilation processes have so far been published.

Based on the hole theory of the positron, the single-quantum process can be interpreted as arising from a radiative transition in which an electron bound in an atom falls into a vacant level in the unoccupied continuous negative-energy state. In this case, as a competitive process there may exist a third process by which a positron annihilates without emission of radiation. This mode of annihilation would occur when the single-quantum annihilation takes place with one of the  $K$ - or  $L$ -shell electrons and when simultaneously the excess energy liberated, instead of being radiated

as a photon, is used to eject another shell electron from the atom concerned. The annihilation by this process, therefore, may be called *radiationless annihilation* or *zero-quantum annihilation*. As is shown in Fig. 1, the energy relation between the incident positron, ejected electron, and a pair of the shell electrons involved is very simple. Let  $E_\alpha$  and  $E_\beta$  be the total energies (including rest mass) of the two bound electrons concerned in the atom before transition, and let  $E_+$  be that of an incident positron; then the total energy  $E_-$  of the electron ejected as a result of the radiationless annihilation is given by

$$E_- = E_+ + E_\alpha + E_\beta. \quad (1)$$

It is noted that the figure and diagram shown in Fig. 1 are concerned with the process where the total energy of a shell electron with which a positron annihilates is denoted by a subscript  $\alpha$  and that of another shell electron before ejection is by a subscript  $\beta$ . Similar figure and diagram are obtained by exchanging  $\alpha$  for  $\beta$  in the case where  $\alpha$  is for the electron to be ejected and  $\beta$  is for the electron with which a positron annihilates. Equation (1) is valid for both of these cases.